Applied Surface Science 433 (2018) 772–779

Contents lists available at ScienceDirect

Applied Surface Science

journal homepage: www.elsevier.com/locate/apsusc

Full Length Article

# Pulsed laser ablation and incubation of nickel, iron and tungsten in liquids and air

N. Lasemi[a], U. Pacher[a], L.V. Zhigilei[a,b], O. Bomatí-Miguel[a,c], R. Lahoz[d], W. Kautek[a,*]

[a] University of Vienna, Department of Physical Chemistry, Währinger Strasse 42, A-1090 Vienna, Austria
[b] University of Virginia, Department of Materials Science & Engineering, PO Box 400745, Charlottesville, VA 22904-4745, USA
[c] Autonomous University of Madrid, Department of Applied Physics, Calle Francisco Tomás y Valiente 7, E-28049 Madrid, Spain
[d] Centro de Química y Materiales de Aragón, University of Zaragoza – CSIC, María de Luna 3, E-50018 Zaragoza, Spain

ARTICLE INFO

*Article history:*
Received 21 April 2017
Received in revised form 10 October 2017
Accepted 11 October 2017
Available online 12 October 2017

*Keywords:*
Laser ablation
Incubation
Metals
Fluid interfaces

ABSTRACT

Incubation effects in the nanosecond laser ablation of metals exhibit a strong dependence on the thermal and mechanical properties of both the target material and the background gas or liquid. The incubation in air is controlled mainly by thermal properties such as the heat of vaporization. In liquid, the correlation of the incubation and the ultimate tensile stress of the metals suggests that incubation may be related to the mechanical impact on the solid material by the cavitation bubble collapse, causing accumulation of voids and cracks in the subsurface region of the ablation craters. At high ultimate tensile stress, however, the low sensitivity to the environment suggests that the mechanical impact is likely to play a negligible role in the incubation. Finally, the correlation between the incubation and the carbon content of alcoholic liquids may be explained by an absorptivity increase of the cavity surfaces due to carbonaceous deposits generated by laser-induced pyrolysis, or by the mechanical impact of long-living bubbles at higher dynamic viscosity of liquids.

© 2017 Elsevier B.V. All rights reserved.

## 1. Introduction

Laser processing in liquids has attracted attention because of potential applications in surface cleaning, etching, welding, drilling, cutting, and micromachining of metals, alloys, polymers, semiconductors, glasses and ceramics [1,2]. Laser ablation of metals in liquids enables the in-situ study of corrosion and repassivation processes [3,4] as well as the production of biocompatible nanoparticles for medical and catalytic applications [5–7]. The pulsed laser generation of colloidal metal nanoparticles (e.g., Ag, Au, Pt, Pd, Cu, Fe, Ni, W) in distilled water and organic solvents attracted much attention in the past two decades [7–17]. The complex mechanism of laser ablation in liquids involves a series of steps extended over many orders of magnitude in time and involving ablation, plasma expansion inside a cavitation bubble, the penetration of condensed nano-sized phases into the liquid, as well as secondary beam-colloid interaction [18–20].

The dependence of ablation rates and threshold fluences on the number of laser pulses and the background medium, the so-called incubation, has not been understood for metals in contrast to dielectric materials. Therefore, this phenomenon needs further investigations as has been endeavoured in this work.

In order to evaluate ablation and incubation phenomena it is necessary to correlate quantitative ablation and incubation data with the physico-chemical properties of the target materials. In the regime of nanosecond-pulse laser interactions, the behaviour of the ablation is generally controlled by optical properties and/or thermal conductivity of the target material. In this case, the threshold fluence can be roughly estimated as follows:

$$F_{th} \approx \Delta U l_{eff}(1\text{-}R)^{-1}, \quad (1)$$

where $\Delta U$ is the energy density needed to heat, melt, and vaporize the target material, $R$ the reflectivity, and $l_{eff}$ is the effective depth of energy deposition [21–23]. In the nanosecond laser interaction with metals, $l_{eff}$ is close to the heat diffusion length $l_T \approx (\delta\tau)^{0.5}$, where $\tau$ is the laser pulse duration, $\delta = \kappa/(\rho c_p)$ the thermal diffusivity of the material, $\kappa$ the thermal conductivity, $\rho$ the density, and $c_p$ the heat capacity. The energy density $\Delta U$ can be approximated by the heat of vaporization, $L_v \times \rho$ (Table 1), which accounts for more than 95% of $\Delta U$ for any material considered in this work.

Nanosecond pulses show higher threshold values than subpicosecond pulses [24–28]. Long pulse durations (≥ns) induce plasma shielding and scattering so that radiation is lost for the absorption process [27], and/or heat diffusion into the bulk materi-

* Corresponding author.
*E-mail address:* wolfgang.kautek@univie.ac.at (W. Kautek).

https://doi.org/10.1016/j.apsusc.2017.10.082
0169-4332/© 2017 Elsevier B.V. All rights reserved.

**Table 1**
Thermal and physical constants of various metals [65]. $T_v$: boiling point; $T_m$: melting point; $c_p$: heat capacity; κ: thermal conductivity; ρ: density; $L_v$: heat of vaporization; $L_m$: heat of melting; δ: heat diffusivity; $R$: reflectivity.

| | $T_v$/K | $T_m$/K | $c_p$/JK$^{-1}$ kg$^{-1}$ | ρ/g cm$^{-3}$ | $L_v$/Jg$^{-1}$ | $L_m$/Jg$^{-1}$ | κ/Wm$^{-1}$ K$^{-1}$ | δ/cm$^2$ s$^{-1}$ | $R_{532nm}$ |
|---|---|---|---|---|---|---|---|---|---|
| Ni | 3005 | 1726 | 444 | 8.90 | 6378 | 292 | 91 | 0.23 | 0.60 |
| Fe | 3023 | 1808 | 444 | 7.87 | 6095 | 272 | 80 | 0.23 | 0.56 |
| W | 5933 | 3683 | 133 | 19.30 | 4009 | 192 | 173 | 0.67 | 0.49 |

als increases, and, thus, the threshold increases as well (acc. to Eq. (1)). The experimental determination of the ablation threshold can be based on the evaluation of the squared diameter of the ablated zone, $D^2$, related to the Gaussian beam radius ($w_0$), the fluence $F$, and the threshold fluence $F_{th}$ with the assumption of a Gaussian beam profile [22,29]:

$$D^2 = 2{w_0}^2 \ln(F/F_{th}). \quad (2)$$

When the ablation exhibits incubation behaviour, the threshold fluence as a function of the number of pulses, $F_{th}(N)$, can be represented as [22,29]

$$F_{th}(N) = F_{th}(1)N^{\xi-1}, \quad (3)$$

where ξ is a material-dependent incubation coefficient, $F_{th}(1)$ is the single shot ablation threshold, and $N$ is the number of pulses. In this simple phenomenological model, it was suggested that the incubation is related to the accumulation of mechanical damage. If ξ = 1, incubation is absent, whereas for values between 0 and 1 the material is weakened by defect accumulation [22,29]. For metals, the factor ξ is typically between 0 and 1. The origin of the incubation in metals is still under debate. It was suggested that incubation might be related to fatigue damages [29,30]. A theoretical expression for the incubation coefficient is not existent, nor is a description of which materials should exhibit a larger incubational behaviour. There have been few attempts to quantify the influence of the target material conversion and structural modification in a multi-pulse experiment by phenomenological [22,29,31–33] and physical models based on reflectivity changes due to roughness evolution at low pulse numbers [34] and bulk defects [35,36]. In the later model, incubation was attributed to high-density defects (HDDs) in the absorption volume of the solid.

The finite incubation of metals in air may be correlated with the formation of voids and/or cracks in the resolidifying layers that remain after the ablation process [7,37,38]. The subsurface regions affected by the void/crack formation are expected to exhibit significantly lower heat diffusion lengths, $l_T$, than the homogeneous bulk material due to strongly reduced heat diffusivities δ. Thus, the heat dissipation is reduced and the ablation threshold decreases (Eq. (1)) with the void accumulation. No incubation investigations exist so far for laser ablation in liquids.

In this work, models considering various materials properties and structural modifications [7,35–38] – beyond the well described optical changes (comp. dielectrics) – are discussed and semi-quantitatively correlated with the observed contrasting incubation behaviour of Ni, Fe, and W in various media.

## 2. Experimental

The target materials were nickel (Alfa Aesar; purity ≥99.5%, 50 × 50 × 2 mm), iron (Goodfellow; purity 99.5%, tempered, round disk, diameter 25 mm, thickness 0.5 mm), and tungsten (Goodfellow; 99.95%, tempered, as rolled, 20 × 20 × 0.5 mm). The liquids were distilled water, ethanol, butanol, and isopropanol (Sigma-Aldrich; p.a.). The metal platelets were cleaned by ultrasonication in ethanol, and were positioned in a glass cell with an optical window allowing the horizontal access of the laser beam. This was focused by a plano-convex lens with a focal length of 92 mm yielding a depth of focus of 1.5 mm. The cell was positioned on a motorized XY-scanning stage. The energy attenuation was performed by a polarizer with a half-wave plate. A power meter (OPHIR Photonics) could be positioned after the polarizer (THORLABS). The focus position in air and various liquid media were experimentally evaluated by microscopically measuring the ablation area on a silicon target (Zeiss AxioVision software) as a function of the distance of the focusing plano-convex lens. A Q-switched Nd:YAG laser system was employed emitting at a wavelength of 532 nm (Spectra Physics GCR-130, ≤1.2 W, pulse duration of 5 ns, repetition rate of 20 Hz, beam diameter of about 5 mm). The images of the modified target regions were recorded by a CCD camera connected to an optical microscope (OLYMPUS, STM-MJS). The recorded ablated areas were evaluated by Zeiss AxioVision software. From this, the average diameter $D$ and $D^2$ were calculated in order to evaluate the ($D^2$-ln$F$)-relationship [22,29]. In order to evaluate the Gaussian beam radius, the so-called cutting edge technique was applied [39,40]. Imaging of various morphologies of the laser-ablated craters was performed by scanning electron microscopy (SEM; Zeiss Supra 55 VP).

## 3. Results and discussion

Laser ablation in various fluids in comparison to air environment was performed at various $F$- and $N$-values. The phenomenon of incubation relies on laser-induced conversion, modification of target microstructure, and phase changes. Therefore, scanning electron microscopy with secondary electron emission (SE-SEM) detection was performed on ablation craters of Ni (Fig. 1) and Fe (Fig. 2) in both water and ethanol, and on W in water (Fig. 3) in comparison to air environment. SE-SEM was chosen to achieve surface-sensitive information (secondary electron escape depth <20 nm) on the morphology and possibly also on conversion products. Charging effects and/or varying secondary electron emission rates can support this analysis [41,42].

The SE-SEM image of a nickel crater generated in air shows strong charging in contrast to the pristine surface of the sample (Fig. 1A). This is indicative of the conversion of Ni to a much thicker $NiO_x$ film inside the crater as compared to the untreated surface. Actually, $NiO_x$ exhibits an extremely low conductivity at room temperature only comparable to fully oxidized iron oxide, $Fe_2O_3$ [43]. When the ablation takes place under water, less formation of $NiO_x$ can be expected. Only few thicker isolated oxide regions appeared as “flakes” in the crater bottom (Fig. 1B). This suggests that the mixture of water and Ni vapour during the bubble lifetime does not provide as much reactive oxygen for a thick coverage of the crater with this low-conductivity $NiO_x$ in contrast to air (Fig. 1A). Actually, gas chromatography showed that during laser ablation in water, water splitting led to both hydrogen and oxygen in the bubbles [44]. Both the presence of hydrogen and the relative shortage of oxygen in the bubble result in the formation of less $NiO_x$ (Fig. 1B) as compared to the air case (Fig. 1A). The ablation crater under ethanol also shows much less charging than in the case of air (Fig. 1A) but still exhibits a pronounced morphology with increased SE emission that is not restricted to the edges (Fig. 1C). That may indicate the formation of conductive non-oxidic conversion phases, such as nickel carbide due to the carbonization of ethanol [44–48]. Further investigations on this issue are under way.

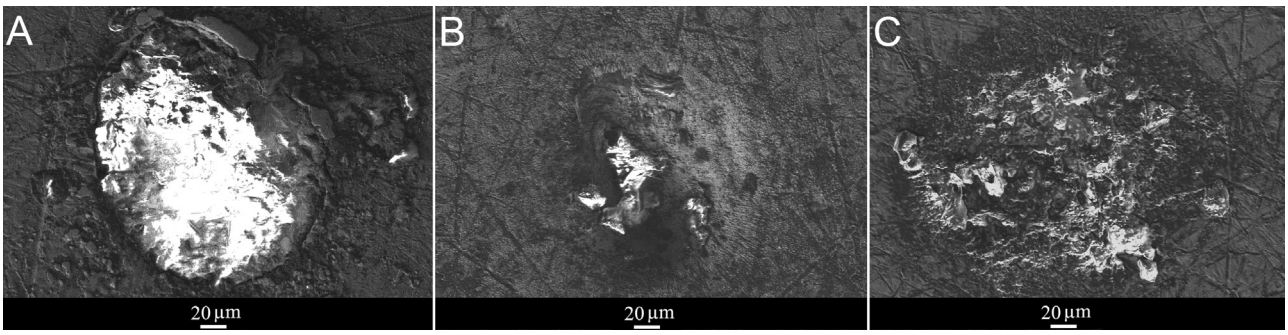


**Fig. 1.** SEM images of Ni ablated craters in various media; A: air ($N = 500$, $F = 310\,Jcm^{-2}$); B: Water ($N = 500$, $F = 400\,Jcm^{-2}$); C: Ethanol ($N = 500$, $F = 400\,Jcm^{-2}$).

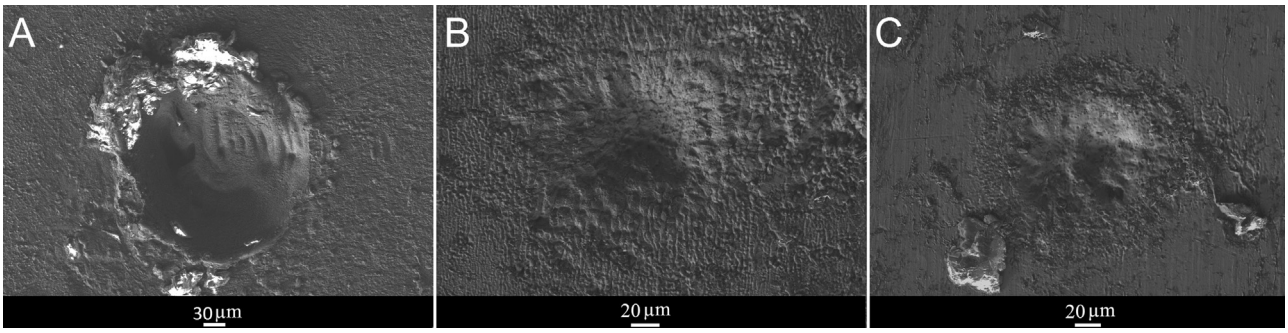


**Fig. 2.** SEM images of Fe ablated craters in various media; A: air ($N = 500$, $F = 310\,Jcm^{-2}$); B: Water ($N = 500$, $F = 400\,Jcm^{-2}$); C: Ethanol ($N = 500$, $F = 400\,Jcm^{-2}$).

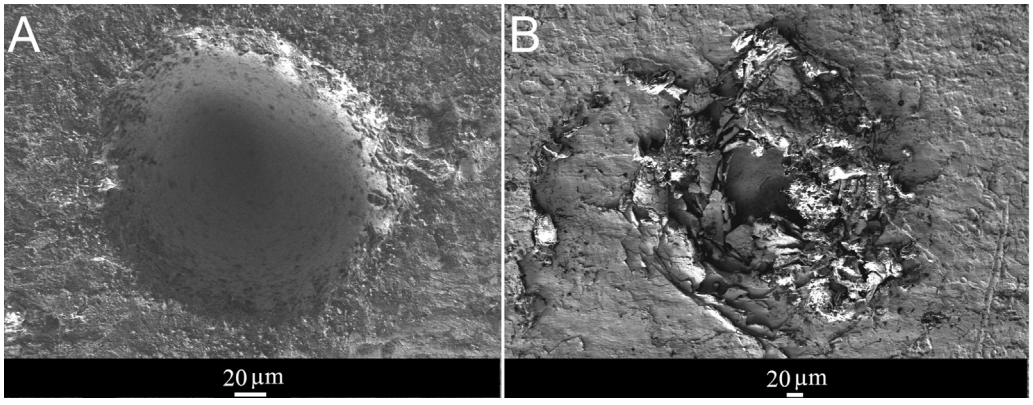


**Fig. 3.** SEM images of W ablated craters in various media; A: air ($N = 100$, $F = 310\,Jcm^{-2}$); B: Water ($N = 100$, $F = 700\,Jcm^{-2}$).

An SE image of an iron ablation crater in air (Fig. 2A) does not exhibit the type of charging as observed with Ni (comp. Fig. 1A). Fe certainly converted to an oxide after laser treatment. Oxidation of iron leads to different iron oxides ($FeO_x$) with various phases such as hematite ($\alpha$-$Fe_2O_3$), maghemite ($\gamma$-$Fe_2O_3$), wüstite (FeO) and magnetite ($Fe_3O_4$). Hematite is the most stable phase of $FeO_x$ with an optical band gap of ~2.2 eV [49–51]. However, the presence of a plasma containing a finite concentration of free electrons may provide a reducing function [52]. Thus, the resulting Fe oxides contain lower oxidation states, e.g. in FeO or $Fe_3O_4$, which show metallic conductivity [43], and therefore no charging in SEM. Apparently, the FeO or $Fe_3O_4$ mixture typical for iron in air has been formed. The exception of this finding is observed at the crater edges, where strongly charged "flakes" appeared (Fig. 2A). Actually, air oxygen could access the heated iron target freely outside the plasma region resulting in completely oxidized iron, i.e. $Fe_2O_3$, which has an at least 20 orders of magnitude lower conductivity than the $Fe^{2+}$ containing oxide phases [43]. The craters under water (Fig. 2B) and ethanol (Fig. 2C) showed no charging suggesting the absence of $Fe_2O_3$, because the fluid confined plasma protected the crater surfaces from complete oxidation, leading only to highly conductive species FeO and $Fe_3O_4$.

Tungsten ablation in air showed no charging of oxide phases (Fig. 3A) both at the edges and in the crater. The crater walls exhibited a smoother morphology than the original target surface due to melting and resolidification followed by oxidation. It should be considered that $WO_3$ under atmospheric conditions is intrinsically 'self-doped' by native oxygen vacancy point defects resulting in coloured $WO_{3-x}$ films with transparencies depending on the level of oxygen vacancies [53–57]. The plasma containment under water led to surface modification by the strong cavitation impact extending outside the irradiated area (Fig. 3B).

The evaluation of the ablation thresholds and the incubation behaviour is based on the measurement of the crater diameters $D$ by optical microscopy and fitting the data points to Eq. (2). In order to document this procedure, but also the collateral modification features around the craters, representative images of the respec-

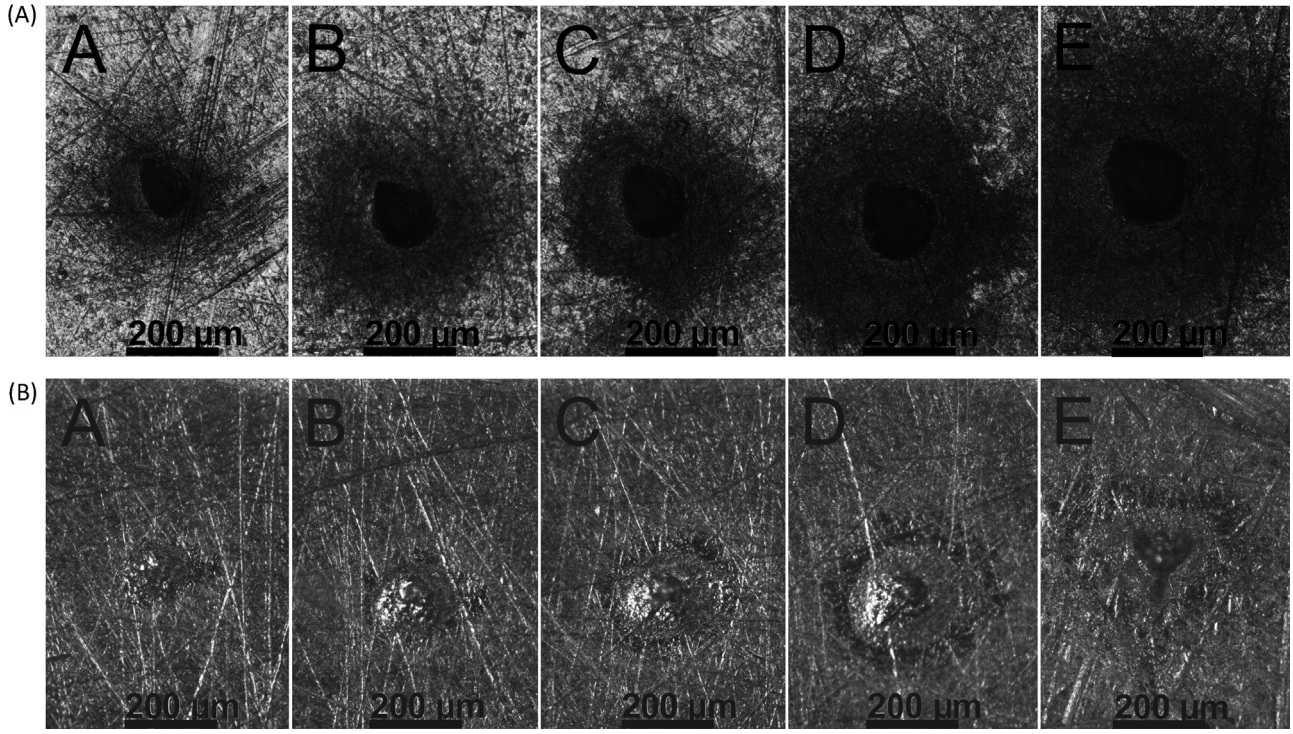


**Fig. 4.** Representative optical micrographs of laser-treated nickel. $N = 500$. a: in water. b: in ethanol. A: $F = 100\,Jcm^{-2}$, B: $F = 200\,Jcm^{-2}$, C: $F = 400\,Jcm^{-2}$, D: $F = 700\,Jcm^{-2}$, E: $F = 1100\,Jcm^{-2}$.

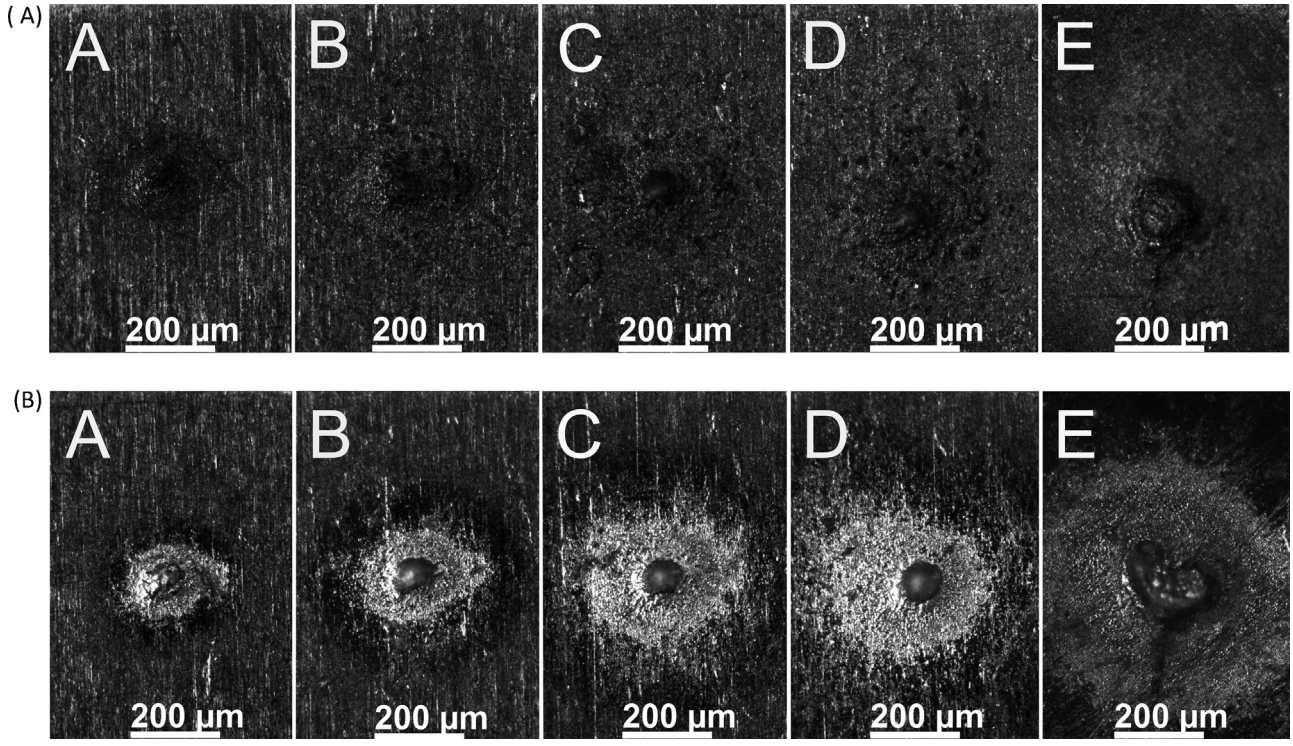


**Fig. 5.** Representative optical micrographs of laser-treated iron. a: in water. b: in ethanol. $N = 500$. A: $F = 100\,Jcm^{-2}$, B: $F = 200\,Jcm^{-2}$, C: $F = 400\,Jcm^{-2}$, D: $F = 700\,Jcm^{-2}$, E: $F = 1100\,Jcm^{-2}$.

tive ablation craters of Ni (Fig. 4) and Fe (Fig. 5) in both water and ethanol, and of W in water (Fig. 6) are presented.

In water, Ni shows a modification zone with reduced reflectivity next to the crater edges increasing with fluence, i.e. from ca. 50 µm at $100\,Jcm^{-2}$ up to ca. 300 µm at 1100 $cm^{-2}$ (Fig. 4a). A closer inspection of the respective SE-SEM image (Fig. 1B) shows no major $NiO_x$ growth within the cavity zone. The origin of this phenomenon is likely to be related to the cavitation bubble dynamics, although the mechanistic details are not yet established. The

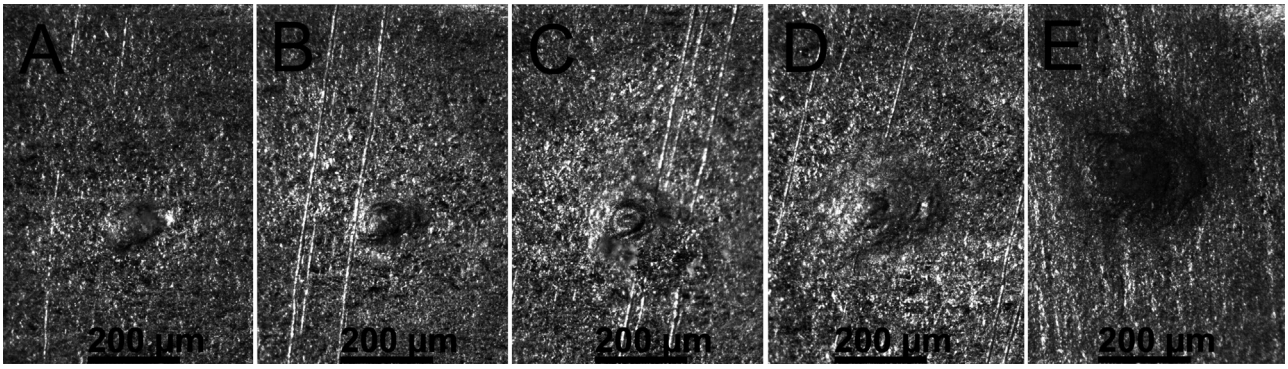


**Fig. 6.** Representative optical micrographs of laser-treated tungsten in water. $N = 100$. A: $F = 100\,Jcm^{-2}$, B: $F = 200\,Jcm^{-2}$, C: $F = 400\,Jcm^{-2}$, D: $F = 700\,Jcm^{-2}$, E: $F = 1100\,Jcm^{-2}$.

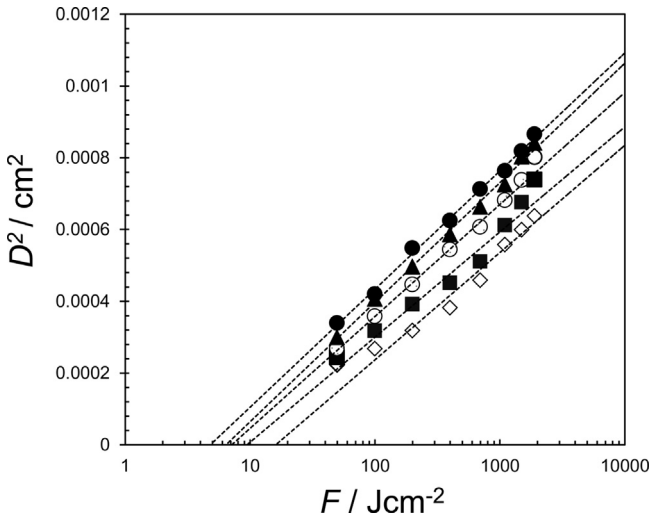


**Fig. 7.** Squared diameter of the ablation area versus pulse fluence ($D^2$ vs $F$; Eq. (2)). Fe in ethanol. ◊: $N = 50$, ■: $N = 100$, ○: $N = 200$, ▲: $N = 500$, ●: $N = 1000$.

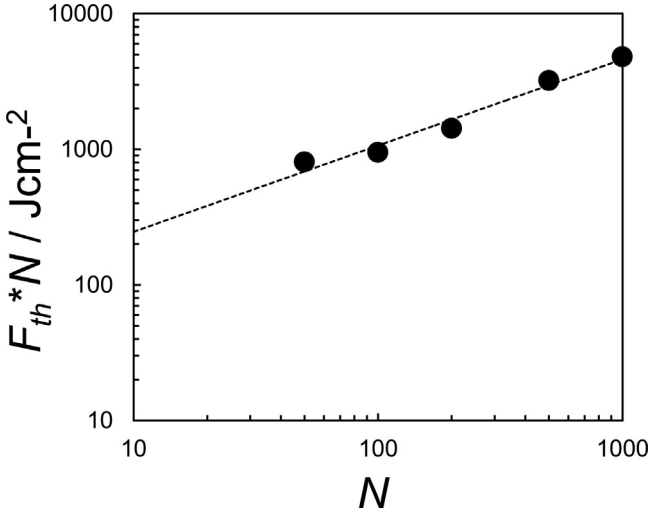


**Fig. 8.** Incubation behaviour of iron in ethanol (acc. Eq. (3)).

zone of reduced reflectance is much smaller in ethanol (Fig. 4b), i.e. <10 µm at 100 $Jcm^{-2}$ up to ca. 50 µm at 1100 $Jcm^{-2}$.

The optical images of craters on Fe in water (Fig. 5a) showed the roughened region outside the craters similarly to the SE-SEM images (Fig. 2B). This kind of cavitation regions in ethanol exhibited higher optical reflectivity (Fig. 5b). Possibly carbonaceous conversion products due to the pyrolysis of ethanol [45–48] may be the cause. The optical images of W craters in water (Fig. 6) show again roughening outside the cavities.

The multi-pulse incubation behaviour quantified by the material-dependent incubation coefficient ξ was evaluated according to Eq. (3) based on a $D^2$-log$F$ evaluation of the values of the threshold fluence (Eq. (2)). Representative results are depicted for Fe in ethanol (Figs. 7 and 8). Due to the difficulties with the evaluation of diameters for shallow craters generated at low pulse numbers $N$ and low fluences, only the data points at higher $N$ and $F$ were considered in fitting to Eq. (2). All evaluated incubation coefficients ξ are presented in Fig. 9. The incubation of the substrates in air depends strongly on the metal type, with Ni exhibiting negligible and W the highest incubation.

All investigated metals exhibit a moderate, but finite incubation in air, i.e. $\xi < 1.0$ (Fig. 9). The incubation in metals may be attributed to the formation and accumulation of voids and/or cracks in the subsurface layer within the laser spot. A porous region generated due to the void formation is expected to exhibit a drastically reduced heat diffusion length $l_T$ and thermal diffusivities δ as compared to the homogeneous bulk material. Thus, the heat dissipation can be reduced and the ablation threshold may decrease (comp. Eq. (1)) due to the sub-surface void accumulation [3,7,37,38]. This qualitative hypothetical model is correlated to a recently developed concept for sub-picosecond laser interactions with metals, where nanovoids are observed to form due to rarefaction processes in the near-surface region of the target [37,58]. Further research on the applicability of this model to the nanosecond irradiation regime is under way.

Ni in air exhibited negligible incubation ($\xi \approx 1$, Fig. 9) suggesting that the before-mentioned qualitative void/crack formation mechanism in the surface-near bulk is of minor importance. In water, however, a substantially higher incubation ($\xi = 0.52$) with respect to air environment is observed. Possible reaction products, such as oxides, should not have a strong effect on the irradiation absorption. Therefore, the possibility of an accumulation of defects, such as voids and cracks (comp. [37,38]), below the cavities due to the cavitation impact under water may be considered as cause for the increased thermal containment with increasing $N$. A contribution of the reduction of the thermal diffusivity by the admixture of oxide phases into the metal matrix may also contribute to the thermal containment.

The comparison of incubation coefficients ξ in water and alcohols, which exhibit strongly varying surface tension γ (22–25 mN $m^{-1}$ for alcohols [59,60] and 72 mN $m^{-1}$ for water), shows a lack of clear correlation between ξ and γ. In contrast to acoustically generated cavitation bubble dynamics [61], laser induced bubbles may be driven by overpressure with minimal contribution from surface tension [62]. However, the estimations of the vapour pressure at the bubble wall based on the values of surface tension and dynamic viscosity of water and alcohols and the equa-

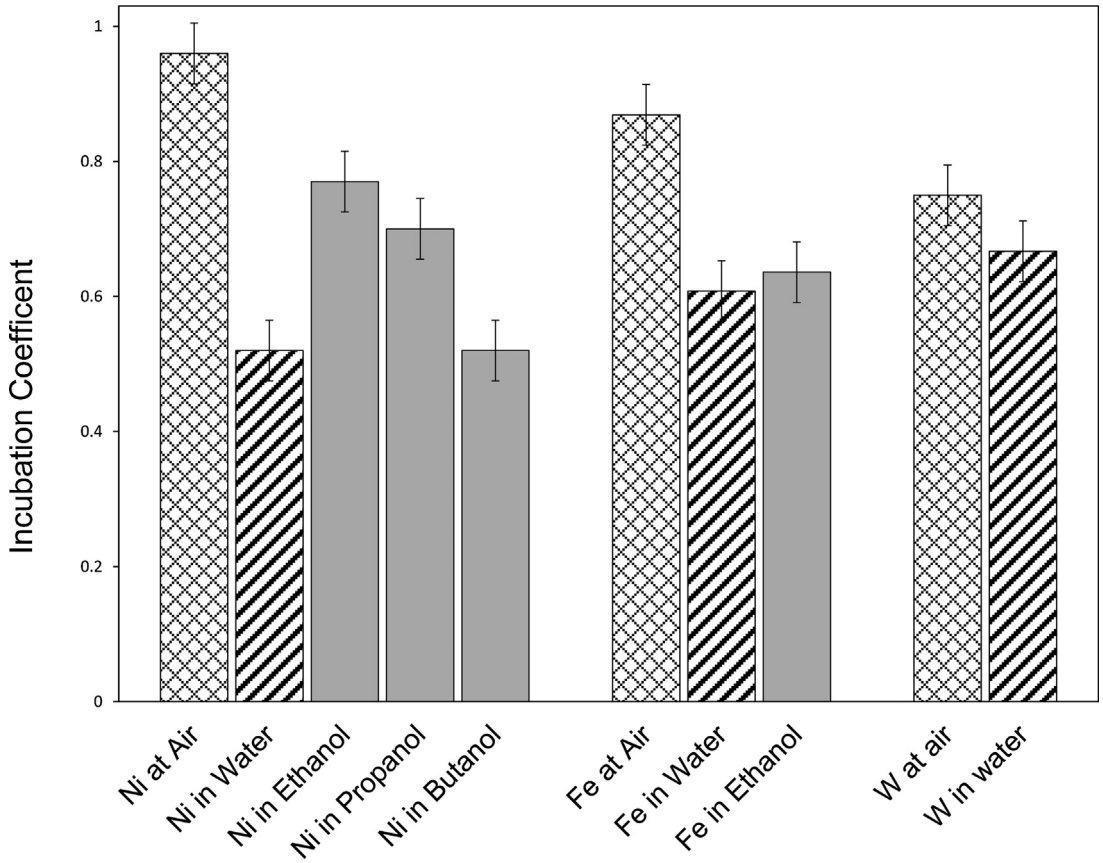


**Fig. 9.** Incubation coefficients in air and various liquids. Ni data from [7].

tion given in Ref. [63] reveals a correlation between the pressure and incubation.

Moreover, the incubation in Ni significantly increased ($\xi$ is reduced) with increasing number of carbon atoms in the alcohol molecules (Fig. 9). Solvents with a higher number of carbon atoms generally show a pyrolysis on hot metal surfaces [45–48]. One can assume that each additional laser pulse leads to more carbonaceous products on the metal target. This is supported by recent $\mu$-Raman experiments to be reported elsewhere [64]. Thus, increasing the absorption at the metal-liquid interface may result in what can be understood as incubation.

Fe in air exhibited a low ($\xi \approx 0.9$) but somewhat higher incubation than Ni (Fig. 9) suggesting that the before-mentioned qualitative void/crack formation mechanism [37,38,58] plays a moderate role. The presence of liquid environment, water or ethanol, led to a substantially higher incubation ($\xi = 0.6$) with respect to air environment. By analogy with Ni, the possibility of an introduction of defects (voids and cracks, comp. [37,38]) below the cavities caused by the cavitation impact may be considered. Thus, the thermal confinement with increasing $N$ may lead to the observed incubation.

W in air (Fig. 7) exhibited the highest incubation ($\xi = 0.75$) of all metals. This finding suggests that the multiple void/crack formation mechanism in the sub-surface region is more effective for W. The presence of water led only to a slight increase in incubation ($\xi = 0.67$) in contrast to the behaviour of Ni and Fe.

Ablation in air is controlled mainly by thermal properties of the metal targets such as the heat of vaporization and the possible formation of voids and cracks near the ablation craters [19,37,38]. Thus, a correlation between the incubation coefficients $\xi$ with the heat of vaporization $L_v$ [66] could be observed (Fig. 10), i.e. a lower $L_v$ supports an increased void formation.

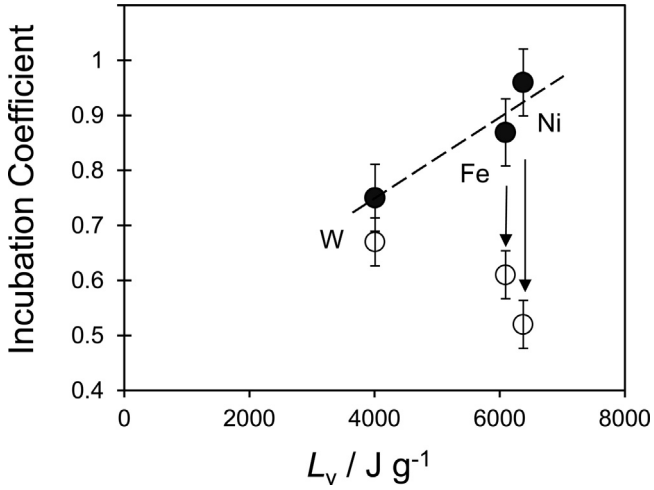


**Fig. 10.** Incubation coefficients versus heat of vaporization $L_v$ (from [65]). ●: in air; ○: in water. The arrows indicate the change of the incubation coefficient upon immersion into water.

The incubation in liquid medium generally increases in comparison with air (Fig. 9). There is practically no correlation of $\xi$ in water with $L_v$ (Fig. 10). However, it is correlated with the strength of mechanical impact on the metals by the bubble cavitation. The extent of the increase of $\xi$ depends strongly on the ultimate tensile stress $\sigma_{TS}$ of the metal [66] (Fig. 11). Incubation of a metal with low $\sigma_{TS}$ (e.g., Ni) shows a drastic $\xi$ decrease (incubation increase) suggesting the thermomechanical nanovoid/crack formation mechanism in the cavitation process. In contrast, the mechanical cavitation mechanism plays a rather negligible role in

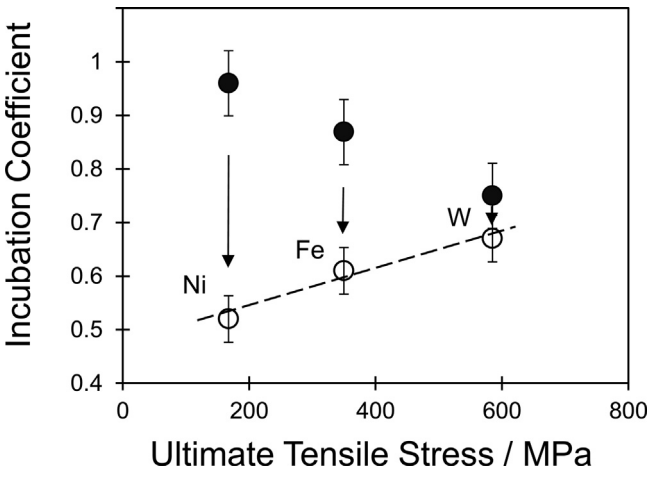


**Fig. 11.** Incubation coefficients versus ultimate tensile stress $\sigma_{TS}$ (from [66]). ●: in air; ○: in water. The arrows indicate the change of the incubation coefficient upon immersion into water.

the incubation in a metal with high $\sigma_{TS}$ (e.g. W) because $\xi$ is almost the same as in air.

A third, optical absorption mechanism may come into play when alcoholic fluids with varying carbon numbers are applied (Fig. 9). An influence of this number on the incubation may suggest a possible absorptivity increase of the cavity surfaces due to carbonaceous deposits generated by laser-induced pyrolysis, particularly at higher carbon contents like in butanol.

## 4. Conclusions

The ablation and incubation of metals in air is correlated with thermal properties such as the heat of vaporization, and may be related to the accumulation of high-density defects such as voids and cracks below the ablation crater surface. The introduction of a liquid medium changes the cause for high-density defects from a thermal to a mechanical due to bubble cavitation impact, as suggested by the correlation of the incubation and the ultimate tensile stress of the metal. In particular, nickel exhibits relatively low ultimate tensile stress and shows the highest incubation increase in a liquid medium. This is in strong contrast to tungsten that has a much higher ultimate tensile stress than nickel and shows an incubation behaviour barely affected by a liquid environment. An optical absorption mechanism may become important when alcohols with varying carbon numbers are applied: the carbon content could affect the tendency to generate carbonaceous deposits by laser-induced pyrolysis thus increasing the incubation.

## Acknowledgements

Partial financial support by the Austrian Science Fund (FWF) through the Lise Meitner Programme (project M 1984), the H2020 Action MSCA-IF 656908-NIMBLIS-ESR, the National Science Foundation through Grant CMMI-1301298, and the MAT2015-67354-R project of the Spanish Ministry of Economy and Competitiveness (MINECO) is gratefully acknowledged.

## References

[1] A. Kruusing, Underwater and water-assisted laser processing: Part 2—Etching, cutting and rarely used methods, Opt. Laser. Eng. 41 (2004) 329–352.
[2] J. Lv, X. Dong, K. Wang, W. Duan, Z. Fan, X. Mei, Study on process and mechanism of laser drilling in water and air, Int. J. Adv. Manuf. Technol. 86 (2016) 1443–1451.
[3] T.O. Nagy, U. Pacher, H. Pöhl, W. Kautek, Atomic emission stratigraphy by laser-induced plasma spectroscopy: quantitative depth profiling of metal thin film systems, Appl. Surf. Sci. 302 (2014) 189–193.
[4] T.O. Nagy, M.J.J. Weimerskirch, U. Pacher, W. Kautek, Repassivation investigations on aluminium: physical chemistry of the passive state, Zeitschrift für Physikalische Chemie 230 (2016) 1303–1327.
[5] S. Barcikowski, G. Compagnini, Advanced nanoparticle generation and excitation by lasers in liquids, Phys. Chem. Chem. Phys. 15 (2013) 3022–3026.
[6] S. Barcikowski, V. Amendola, G. Marzun, C. Rehbock, S. Reichenberger, D. Zhang, B. Gökce, Handbook of Laser Synthesis of Colloids, 2016.
[7] N. Lasemi, U. Pacher, C. Rentenberger, O. Bomatí-Miguel, W. Kautek, Laser-assisted synthesis of colloidal Ni/NiOx core/shell nanoparticles in water and alcoholic solvents, ChemPhysChem 18 (2017) 1118–1124.
[8] F. Mafune, Y. Kohno, T. Kondow, H. Sawabe, Formation and size control of silver nanoparticles by laser ablation in aqueous solution, J. Phys. Chem. B 104 (2000) 9111–9117.
[9] V.K. Pavel, V.V. Valerii, V.S. Aleksandr, A.S. Georgii, Production of copper and brass nanoparticles upon laser ablation in liquids, Quantum. Electron. 34 (2004) 951.
[10] M.S.F. Lima, F.P. Ladário, R. Riva, Microstructural analyses of the nanoparticles obtained after laser irradiation of Ti and W in ethanol, Appl. Surf. Sci. 252 (2006) 4420–4424.
[11] W.T. Nichols, T. Sasaki, N. Koshizaki, Laser ablation of a platinum target in water. I. Ablation mechanisms, J. Appl. Phys. 100 (2006) 114911.
[12] V. Amendola, P. Riello, S. Polizzi, S. Fiameni, C. Innocenti, C. Sangregorio, M. Meneghetti, Magnetic iron oxide nanoparticles with tunable size and free surface obtained via a green approach based on laser irradiation in water, J. Mater. Chem. 21 (2011) 18665–18673.
[13] C. Rehbock, V. Merk, L. Gamrad, R. Streubel, S. Barcikowski, Size control of laser-fabricated surfactant-free gold nanoparticles with highly diluted electrolytes and their subsequent bioconjugation, Phys. Chem. Chem. Phys. 15 (2013) 3057–3067.
[14] N. Haram, N. Ahmad, Effect of laser fluence on the size of copper oxide nanoparticles produced by the ablation of Cu target in double distilled water, Appl. Phys. A 111 (2013) 1131–1137.
[15] H.J. Jung, M.Y. Choi, Specific solvent produces specific phase Ni nanoparticles: a pulsed laser ablation in solvents, J. Phys. Chem. C 118 (2014) 14647–14654.
[16] M. Boutinguiza, M. Meixus, J. del Val, A. Riveiro, R. Comesaña, F. Lusquiños, J. Pou, Synthesis and characterization of Pd nanoparticles by laser ablation in water using nanosecond laser, Phys. Procedia 83 (2016) 36–45.
[17] C. Gellini, F.L. Deepak, M. Muniz-Miranda, S. Caporali, F. Muniz-Miranda, A. Pedone, C. Innocenti, C. Sangregorio, Magneto-plasmonic colloidal nanoparticles obtained by laser ablation of nickel and silver targets in water, J. Phys. Chem. C 121 (2017) 3597–3606.
[18] J. Lam, D. Amans, F. Chaput, M. Diouf, G. Ledoux, N. Mary, K. Masenelli-Varlot, V. Motto-Ros, C. Dujardin, γ-$Al_2O_3$ nanoparticles synthesised by pulsed laser ablation in liquids: a plasma analysis, Phys. Chem.Chem. Phys. 16 (2014) 963–973.
[19] C.-Y. Shih, C. Wu, M.V. Shugaev, L.V. Zhigilei, Atomistic modeling of nanoparticle generation in short pulse laser ablation of thin metal films in water, J. Colloid Interface Sci. 489 (2017) 3–17.
[20] S. Reich, P. Schönfeld, P. Wagener, A. Letzel, S. Ibrahimkutty, B. Gökce, S. Barcikowski, A. Menzel, T. dos Santos Rolo, A. Plech, Pulsed laser ablation in liquids: impact of the bubble dynamics on particle formation, J. Colloid Interface Sci. 489 (2017) 106–113.
[21] E. Matthias, M. Reichling, J. Siegel, O.W. Käding, S. Petzoldt, H. Skurk, P. Bizenberger, E. Neske, The influence of thermal diffusion on laser ablation of metal films, Appl. Phys. A 58 (1994) 129–136.
[22] J. Krüger, W. Kautek, Ultrashort pulse laser interaction with dielectrics and polymers, Adv. Polym. Sci. 168 (2004) 247–289.
[23] M. Forster, L. Égerházi, C. Haselberger, C. Huber, W. Kautek, Femtosecond laser interaction with pulsed-laser deposited carbon thin films of nanoscale thickness, Appl. Phys. A 102 (2011) 27–33.
[24] P.K. Kennedy, S.A. Boppart, D.X. Hammer, B.A. Rockwell, G.D. Noojin, W.P. Roach, A first-order model for computation of laser-induced breakdown thresholds in ocular and aqueous media. II. Comparison to experiment, IEEE J. Quantum Electron. 31 (1995) 2250–2257.
[25] J. Noack, A. Vogel, Laser-induced plasma formation in water at nanosecond to femtosecond time scales: calculation of thresholds, absorption coefficients, and energy density, IEEE J. Quantum Electron. 35 (1999) 1156–1167.
[26] A. Vogel, J. Noack, K. Nahen, D. Theisen, S. Busch, U. Parlitz, D.X. Hammer, G.D. Noojin, B.A. Rockwell, R. Birngruber, Energy balance of optical breakdown in water at nanosecond to femtosecond time scales, Appl. Phys. B 68 (1999) 271–280.
[27] D. Bäuerle, Laser Processing and Chemistry, 4 ed., Springer-Verlag, Berlin Heidelberg, 2011.
[28] K.C. Phillips, H.H. Gandhi, E. Mazur, S.K. Sundaram, Ultrafast laser processing of materials: a review, Adv. Opt. Photonics 7 (2015) 684–712.
[29] Y. Jee, M.F. Becker, R.M. Walser, Laser-induced damage on single-crystal metal surfaces, J. Opt. Soc. Am. B 5 (1988) 648–659.
[30] A. Fatemi, L. Yang, Cumulative fatigue damage and life prediction theories: a survey of the state of the art for homogeneous materials, Int. J. Fatigue 20 (1998) 9–34.
[31] J. Byskov-Nielsen, J.-M. Savolainen, M.S. Christensen, P. Balling, Ultra-short pulse laser ablation of metals: threshold fluence, incubation coefficient and ablation rates, Appl. Phys. A 101 (2010) 97–101.

[32] F. Di Niso, C. Gaudiuso, T. Sibillano, F.P. Mezzapesa, A. Ancona, P.M. Lugarà, Role of heat accumulation on the incubation effect in multi-shot laser ablation of stainless steel at high repetition rates, Opt. Express 22 (2014) 12200–12210.
[33] B. Neuenschwander, B. Jaeggi, M. Schmid, G. Hennig, Surface structuring with ultra-short laser pulses: basics, limitations and needs for high throughput, Phys. Procedia 56 (2014) 1047–1058.
[34] T. Häfner, J. Heberle, M. Dobler, M. Schmidt, Influences on incubation in ps laser micromachining of steel alloys, J. Laser Appl. 28 (2016) 022605.
[35] A. Naghilou, O. Armbruster, M. Kitzler, W. Kautek, Merging spot size and pulse number dependence of femtosecond laser ablation thresholds: modeling and demonstration with high impact polystyrene, J. Phys. Chem. C 119 (2015) 22992–22998.
[36] A. Naghilou, O. Armbruster, W. Kautek, Femto- and nanosecond pulse laser ablation dependence on irradiation area: the role of defects in metals and semiconductors, Appl. Surf. Sci. 418 (2017) 487–490.
[37] C. Wu, M.S. Christensen, J.-M. Savolainen, P. Balling, L.V. Zhigilei, Generation of subsurface voids and a nanocrystalline surface layer in femtosecond laser irradiation of a single-crystal Ag target, Phys. Rev. B 91 (2015) 035413.
[38] E.T. Karim, M.V. Shugaev, C. Wu, Z. Lin, H. Matsumoto, M. Conneran, J. Kleinert, R.F. Hainsey, L.V. Zhigilei, Experimental characterization and atomistic modeling of interfacial void formation and detachment in short pulse laser processing of metal surfaces covered by solid transparent overlayers, Appl. Phys. A 122 (2016) 407.
[39] R. Diaz-Uribe, M. Rosete-Aguilar, R. Ortega-Martinez, Position sensing of a Gaussian beam with a power meter and a knife edge, Rev. Mex. Fis. (1993) 484–492.
[40] M. González-Cardel, P. Arguijo, R. Díaz-Uribe, Gaussian beam radius measurement with a knife-edge: a polynomial approximation to the inverse error function, Appl. Opt. 52 (2013) 3849–3855.
[41] K.H. Kim, Z. Akase, T. Suzuki, D. Shindo, Charging effects on SEM/SIM contrast of metal/insulator system in various metallic coating conditions, Mater. Trans. 51 (2010) 1080–1083.
[42] P. Li, S.X. Bao, D.Z. Zhang, L.B. Zhuang, L.L. Ma, Application of secondary electron composition contrast imaging method in microstructure studies on cathode materials of TWT, Mater. Sci. Forum 689 (2011) 255–259.
[43] R. Waser, in: H. Schaumburg (Ed.), Lineare und nicht-lineare Widerstände, Keramik, Vieweg + Teubner Verlag, Wiesbaden, 1994, pp. 129–218.
[44] M.-R. Kalus, N. Barsch, R. Streubel, E. Gokce, S. Barcikowski, B. Gokce, How persistent microbubbles shield nanoparticle productivity in laser synthesis of colloids – quantification of their volume, dwell dynamics, and gas composition, Phys. Chem. Chem. Phys. 19 (2017) 7112–7123.
[45] V. Amendola, G.A. Rizzi, S. Polizzi, M. Meneghetti, Synthesis of gold nanoparticles by laser ablation in toluene: quenching and recovery of the surface plasmon absorption, J. Phys. Chem. B 109 (2005) 23125–23128.
[46] H.Y. Kwong, M.H. Wong, C.W. Leung, Y.W. Wong, K.H. Wong, Formation of core/shell structured cobalt/carbon nanoparticles by pulsed laser ablation in toluene, J. Appl. Phys. 108 (2010) 034304.
[47] V. Amendola, P. Riello, M. Meneghetti, Magnetic nanoparticles of iron carbide, iron oxide, iron@iron oxide, and metal iron synthesized by laser ablation in organic solvents, J. Phys. Chem. C 115 (2011) 5140–5146.
[48] V. Amendola, M. Meneghetti, What controls the composition and the structure of nanomaterials generated by laser ablation in liquid solution? Phys. Chem. Chem. Phys. 15 (2013) 3027–3046.
[49] M.A. Aegerter, M. Mennig, Sol-Gel Technologies for Glass Producers and Users, Springer, New York, 2004.
[50] Z.N. Kayani, E.S. Khan, F. Saleemi, S. Riaz, S. Naseem, Optical and magnetic properties of iron oxide thin films, Mater. Today Proc. 2 (2015) 5568–5571.
[51] S. Phokha, S. Pinitsoontorn, S. Rujirawat, S. Maensiri, Polymer pyrolysis synthesis and magnetic properties of LaFeO3 nanoparticles, Physica B 476 (2015) 55–60.
[52] P. Pouli, D.C. Emmony, C.E. Madden, I. Sutherland, Analysis of the laser-induced reduction mechanisms of medieval pigments, Appl. Surf. Sci. 173 (2001) 252–261.
[53] T. He, J. Yao, Photochromic materials based on tungsten oxide, J. Mater. Chem. 17 (2007) 4547–4557.
[54] M. Acosta, D. González, I. Riech, Optical properties of tungsten oxide thin films by non-reactive sputtering, Thin Solid Films 517 (2009) 5442–5445.
[55] D.B. Migas, V.L. Shaposhnikov, V.N. Rodin, V.E. Borisenko, Tungsten oxides. I. Effects of oxygen vacancies and doping on electronic and optical properties of different phases of WO3, J. Appl. Phys. 108 (2010) 093713.
[56] X. He, Y. Yin, J. Guo, H. Yuan, Y. Peng, Y. Zhou, D. Zhao, K. Hai, W. Zhou, D. Tang, Memristive properties of hexagonal WO3 nanowires induced by oxygen vacancy migration, Nanoscale Res. Lett. 8 (2013) 50.
[57] K. Aguir, C. Lemire, D.B.B. Lollman, Electrical properties of reactively sputtered WO3 thin films as ozone gas sensor, Sens. Actuators B: Chem. 84 (2002) 1–5.
[58] J.-M. Savolainen, M.S. Christensen, P. Balling, Material swelling as the first step in the ablation of metals by ultrashort laser pulses, Phys. Rev. B 84 (2011) 193410.
[59] R.E. Bolz, G.L. Tuve, CRC Handbook of Tables for Applied Engineering Science, 2 ed., 1973.
[60] R.C. Weast, Handbook of Chemistry and Physics, 64 ed., CRC Press, 1984.
[61] C.E. Brennen, Cavitation and Bubble Dynamics, Oxford University Press, Oxford, 1995.
[62] J. Lam, J. Lombard, C. Dujardin, G. Ledoux, S. Merabia, D. Amans, Dynamical study of bubble expansion following laser ablation in liquids, Appl. Phys. Lett. 108 (2016) 074104.
[63] I. Akhatov, O. Lindau, A. Topolnikov, R. Mettin, N. Vakhitova, W. Lauterborn, Collapse and rebound of a laser-induced cavitation bubble, Phys. Fluids 13 (2001) 2805–2819.
[64] R. Lahoz, A. Mayoral, G.F. de la Fuente, C. Rentenberger, D. Díaz-Fernández, L. Soriano, W. Kautek, O. Bomati-Miguel, (in publication).
[65] D.R. Lide, H.P.R. Frederikse, Handbook of Chemistry and Physics, 76 ed., CRC Press Boca Raton, FL, 1995–1996.
[66] A.M. Howatson, P.G. Lund, J.D. Todd, Properties of matter, Engineering Tables and Data, Springer, Netherlands, Dordrecht, 1972, pp. 41.